Comparative immune profiling of acute respiratory distress syndrome patients with or without SARS-CoV2 infection

Mikaël Roussel, J. Ferrant, F. Reizine, S. Le Gallou, J. Dulong, S. Carl, M. Lesouhaitier, M. Gregoire, N. Bescher, C. Verdy, et al.

Journal Pre-proof

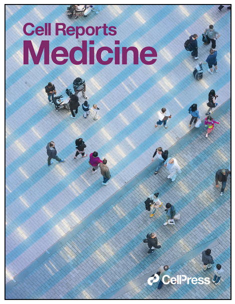

Comparative immune profiling of acute respiratory distress syndrome patients with or without SARS-CoV2 infection

M. Roussel, J. Ferrant, F. Reizine, S. Le Gallou, J. Dulong, S. Carl, M. Lesouhaitier, M. Gregoire, N. Bescher, C. Verdy, M. Latour, I. Bézier, M. Cornic, A. Vinit, C. Monvoisin, B. Sawitzki, S. Leonard, S. Paul, J. Feuillard, R. Jeannet, T. Daix, V.K. Tiwari, J.M. Tadié, M. Cogné, K. Tarte

PII: S2666-3791(21)00119-1

DOI: https://doi.org/10.1016/j.xcrm.2021.100291

Reference: XCRM 100291

To appear in: *Cell Reports Medicine*

Received Date: 3 December 2020

Revised Date: 14 March 2021

Accepted Date: 29 April 2021

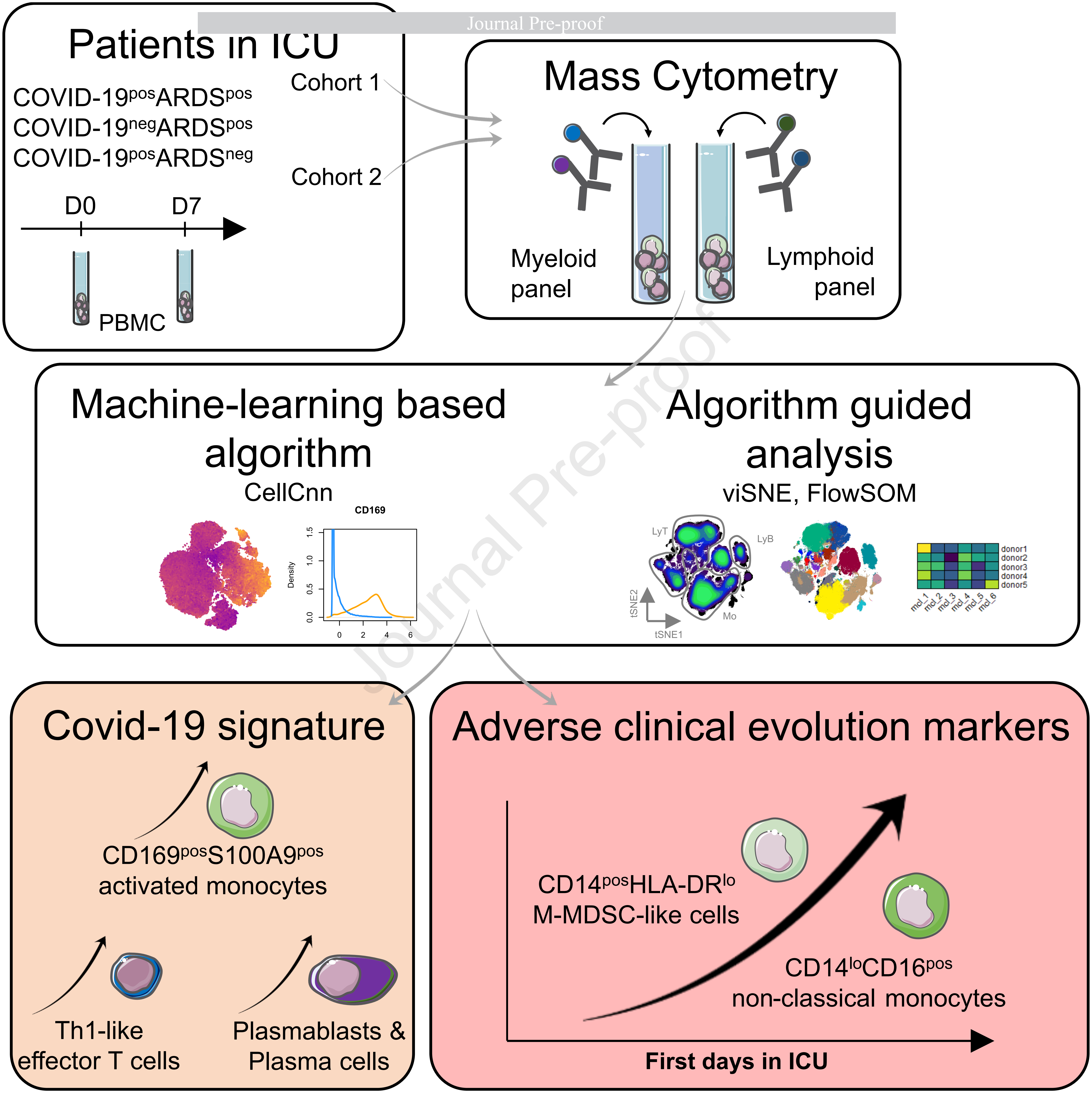
Patients in ICU
COVID-19posARDSpos
COVID-19negARDSpos
COVID-19posARDSneg
Cohort 1
Cohort 2
D0
D7
PBMC
Mass Cytometry
Myeloid panel
Lymphoid panel
Machine-learning based algorithm
CellCnn
CD169
Density
Algorithm guided analysis
viSNE, FlowSOM
LyT
LyB
Mo
tSNE2
tSNE1
Covid-19 signature
CD169posS100A9pos activated monocytes
Th1-like effector T cells
Plasmablasts & Plasma cells
Adverse clinical evolution markers
CD14posHLA-DRlo M-MDSC-like cells
CD14loCD16pos non-classical monocytes
First days in ICU

Comparative immune profiling of acute respiratory distress syndrome patients with or without SARS-CoV2 infection

M. Roussel[1,2,3,16,17]*, J. Ferrant[3,16], F. Reizine[3,4], S. Le Gallou[2,3], J. Dulong[2,3], S. Carl[5], M. Lesouhaitier[3,4], M. Gregoire[2,3], N. Bescher[2], C. Verdy[2], M. Latour[2], I. Bézier[2], M. Cornic[2], A. Vinit[6], C. Monvoisin[3], B. Sawitzki[7], S. Leonard[1], S. Paul[8], J. Feuillard[9], R. Jeannet[9,10,11], T. Daix[11,12,13], V.K. Tiwari[5,14], J.M. Tadié[3,4], M. Cogné[3,15,16], K. Tarte[2,3,16]*

[1]Centre Hospitalier Universitaire de Rennes, Laboratoire Hématologie, Pôle Biologie, F-35033, Rennes, France

[2]Centre Hospitalier Universitaire de Rennes, SITI, Pôle Biologie, F-35033, Rennes, France

[3]Institut national de la santé et de la recherche médicale, Unité Mixte de Recherche U1236, LabEx IGO, Université Rennes 1, Etablissement Français du Sang Bretagne, F-35000, Rennes, France

[4]Centre Hospitalier Universitaire de Rennes, Maladies Infectieuses et Réanimation Médicale, F-35033, Rennes, France

[5]Scailyte AG, CH-6210, Sursee, Switzerland

[6]Sorbonne Université, UMS037, PASS, Plateforme de Cytométrie de la Pitié-Salpêtrière CyPS, F-75013, Paris, France

[7]Charité - Universitätsmedizin Berlin, Institut für Medizinische Immunologie, AG Molekulare Immunmodulation, D-13353, Berlin, Germany

[8]Centre Hospitalier Universitaire de Saint-Etienne, Laboratoire Immunologie, F-42000, Saint-Etienne, France

[9]Centre Hospitalier Universitaire de Limoges, Laboratoire Hématologie, F-87000, Limoges, France

[10]Unité Mixte de Recherche CNRS 7276 INSERM 1262, F-87000, Limoges, France

[11]Centre d'investigation Clinique INSERM 1435, F-87000, Limoges, France

[12]Unité Mixte de Recherche INSERM 1092, F-87000, Limoges, France

[13]Centre Hospitalier Universitaire de Limoges, Service de Réanimation Médicale, F-87000, Limoges, France

[14]Wellcome-Wolfson Institute for Experimental Medicine, School of Medicine, Dentistry & Biomedical Science, Queens University Belfast, BT9 7BL, United Kingdom

[15]Centre Hospitalier Universitaire de Rennes, Laboratoire Immunologie, Pôle Biologie, F-35033, Rennes, France

[16] These authors contributed equally

[17]Lead contact

*Correspondence to: mikael.roussel@chu-rennes.fr (M.R.); karin.tarte@univ-rennes1.fr (K.T.)

Summary

Acute respiratory distress syndrome (ARDS) is the main complication of COVID-19, requiring admission to Intensive Care Unit (ICU). Despite extensive immune profiling of COVID-19 patients, to what extent COVID-19-associated ARDS differs from other causes of ARDS remains unknown. To address this question, we build 3 cohorts of patients categorize in COVID-19^{neg}ARDS^{pos}, COVID-19^{pos}ARDS^{pos}, and COVID-19^{pos}ARDS^{neg}, and compare their immune landscape analyze by high-dimensional mass cytometry on peripheral blood. A cell signature associating S100A9/calprotectin-producing CD169^{pos} monocytes, plasmablasts, and Th1 cells is found in COVID-19^{pos}ARDS^{pos}, unlike COVID-19^{neg}ARDS^{pos} patients. Moreover, this signature is essentially share with COVID-19^{pos}ARDS^{neg} patients, suggesting that severe COVID-19 patients, whatever they experience or not ARDS, display similar immune profiles. We show an increase in CD14^{pos}HLA-DR^{low} and CD14^{low}CD16^{pos} monocytes correlate to the occurrence of adverse events during ICU stay. We demonstrate that COVID-19-associated ARDS display a specific immune profile, and might benefit from personalize therapy in addition to standard ARDS management.

Introduction

The SARS-Coronavirus-2 (SARS-CoV-2) virus has rapidly affected more than 30 million people worldwide, requiring admission to Intensive Care Unit (ICU) for more than 2 million patients.[1] Whereas most patients exhibit mild-to-moderate symptoms, acute respiratory distress syndrome (ARDS) is the major complication of the coronavirus disease 2019 (COVID-19),[2,3] leading to prolonged ICU stays, and high frequency of secondary complications, notably cardiovascular events, thrombosis, pulmonary embolisms, and strokes.[1,4] The immune system plays a dual role in COVID-19, contributing to both virus elimination and ARDS development.[5] Excessive inflammatory response has been proposed as the leading cause of COVID-19-related clinical complications, thus supporting intensive efforts to better understand the specificities and mechanisms of SARS-CoV-2-induced immune dysfunction.[6,7] Moreover, even if therapies such as provided by convalescent plasma or neutralizing antibodies at an early stage of the disease, can lower the viral burden, this was only demonstrated in specific populations such as aged patients over 75,[8] and no antiviral treatment has yet been able to definitely prevent the evolution of some patients towards deregulated inflammation and critical respiratory complications. The benefit of corticosteroids in severe COVID-19 for lowering overall mortality is now widely acknowledged.[9,10] Conversely, steroid therapy was shown harmful in other ARDS etiologies, such as in influenza-associated ARDS,[11] suggesting specific biological features of COVID 19-related ARDS. A detailed understanding of the COVID-19-specific immune dysfunctions underlying ARDS development and severity is thus a major need and will hopefully help adapt specific therapeutic strategy.

A number of high-resolution studies have recently concentrated on the determination of circulating markers that can distinguish severe from mild forms of COVID-19, providing a tremendous amount of data describing phenotypic and functional alterations in T cell, B cell, and myeloid cell subsets.[12–25] In particular, CD14^{pos}HLA-DR^{low}, CD14^{pos}CD16^{pos}, and immature monocytes were demonstrated as increased among peripheral blood mononuclear cells (PBMCs) from critically ill COVID-19 patients.[15,21,23,26–29] Interestingly, monocyte number is reduced in COVID-19 compared to influenza patients, suggesting specific myeloid dysregulation.[30] Various COVID 19-related alterations of lymphoid cells have also been described, including a T-cell lymphopenia, predictive of patient outcome, a broad T-cell activation including Th1, Th2, and Th17, an alteration of B-cell and T-cell repertoires, and a strong increase of plasmablasts, most prominent in ARDS COVID-19 patients.[14,17,25,31–33] Importantly, COVID-19 ARDS immune profiling was performed using healthy donors as a control, thus precluding any conclusions on whether reported immune alterations could be related to COVID-19 and/or ARDS status. Answering this question has potential to decipher whether ARDS induced by SARS-CoV-2 is mechanistically different from other ARDS etiologies.

To fill this gap, we performed a high-throughput mass cytometry approach on PBMCs obtained from 3 complementary series of 18 COVID-19^{neg}ARDS^{pos}, 18 COVID-19^{pos}ARDS^{pos}, and 20 COVID-19^{pos}ARDS^{neg} patients, including exploratory and validation cohorts. We report common myeloid cell alterations in all COVID-19 patients, which are absent from non-COVID-19 ARDS patients. This includes in particular a strong increase of an unusual population of activated monocytes showing upregulated expression of CD169, associated with major COVID-19-specific alterations of T and B-cell compartments.

Results

Study population

Analyses were performed on a cohort 1 of 63 cryopreserved PBMC samples isolated from 42 patients included in ICU (n = 36) or infectious standard ward (n = 6). The demographic characteristics of patients included are provided in Table 1 and Table S1. All patients but one were classified as severe at admission, requiring oxygen at a flow rate higher than 2 liters/min. ARDS was defined in accordance with international guidelines.[34] Patients were classified in 3 groups: COVID-19^{neg}ARDS^{pos} (n = 12, ARDS stages: 1 mild, 4 moderate, 7 severe), COVID-19^{pos}ARDS^{pos} (n = 13, ARDS stages: 8 moderate, 5 severe), and COVID-19^{pos}ARDS^{neg} (n = 17, including 11 from ICU and 6 from infectious standard ward). In the COVID-19^{pos}ARDS^{neg}, no statistical differences were noticed for immune cell abundance or phenotype between ICU and standard ward patients. Within the COVID-19^{neg}ARDS^{pos} group, ARDS etiologies were bacterial pneumonia (n = 9), anti-synthetase syndrome (n = 1), and unknown (n = 2) (Table S1). For 21 patients, a second blood sample obtained on day 7 after enrollment was studied (n = 7 for COVID-19^{neg}ARDS^{pos}, n = 8 for COVID-19^{pos}ARDS^{pos}, and n = 6 for COVID-19^{pos}ARDS^{neg}). Additionally, a validation cohort (cohort 2) was set up with 16 patients with demographic data detailed in Table S1 and Table S2. Patients were classified in 3 groups: COVID-19^{neg}ARDS^{pos} (n = 6), COVID-19^{pos}ARDS^{pos} (n = 5), and COVID-19^{pos}ARDS^{neg} (n = 3); additionally, COVID-19^{neg}ARDS^{neg} (n = 2) samples were included. None of our patients received corticosteroids at the time of the study nor immune-modulators. The presence of SARS-CoV-2 in respiratory specimens (nasal and pharyngeal swabs or sputum) was detected by real-time reverse transcription polymerase chain reaction (RT-PCR) methods. To rule out undetected infections, negative RT-PCR samples were confirmed when possible by absence of neutralizing antibodies. Neutralizing antibodies were undetectable for the 11 samples out of 18 COVID-19^{neg} patients for which material was available. In contrast, neutralizing antibodies were detected in 29 out of 30 COVID-19^{pos} tested. Timeline of sample collection are shown in Fig. S1.

SARS-CoV2 induces phenotypic changes in circulating immune cells

To decipher the impact of SARS-CoV2 on circulating immune cells, we characterized PBMCs from COVID-19^{pos} *versus* COVID-19^{neg} patients at admission using two separate mass cytometry panels exploring myeloid and lymphoid subsets, respectively (Table S3 and Key Resources Table). The full pipeline of analysis is depicted in Fig. S1. First, we performed an unbiased discovery approach with CellCnn, a neural network-based artificial intelligence algorithm allowing analysis of single-cell data and detection of cells associated with clinical status.[35–37] During training, CellCnn learns combinations of weights for each marker in a given panel that best discriminate between groups of patients. These weight combinations, called filters, can be used to highlight the specific profiles of cells associated with patient status. We identified the best-performing CellCnn filters for both the myeloid and the lymphoid panels highlighting a population of cells significantly enriched in COVID-19^{pos} patients as compared to COVID-19^{neg} patients ($P < 0.0001$ for both panels) (Fig. 1A). Projecting these cells on tSNE maps generated with either the myeloid or the lymphoid panels revealed that they fell into several distinct areas (Fig. 1B). The cells selected by the CellCnn filter on the myeloid panel showed high expression for CD169, CD64, S100A9, CD11b, CD33, CD14, and CD36 compared to background, while the cells selected by the CellCnn filter on the lymphoid panel showed high expression for CD38 and CXCR3 (Fig.1B and Fig. S2). These results were replicated in the cohort 2 (Fig. S3), and confirmed on a public set of data by using the CellCnn analysis showing a high expression of CD14, CD36, CD64, and CD169 cells on COVID-19^{pos} patients (Fig. S4).[15] As a whole, this broad and unbiased approach reproducibly showed that immune markers, in particular related to monocytes, segregated COVID-19^{neg} and COVID-19^{pos} patients.

SARS-CoV2 induces CD169-expressing monocyte subsets

To investigate circulating monocyte heterogeneity and define consistent phenotypes, we used the FlowSOM algorithm. This approach led to the identification of 15 monocyte metaclusters from the myeloid panel (Fig. 2A). In particular, Mo30, Mo11, and Mo28 metaclusters were defined by higher expression of CD16 and lower expression of CD14, CD36, and CD64, corresponding to a non-classical monocyte phenotype. Mo21 and Mo22 were defined by the high expression of S100A9 and the low expression of CD36. Finally, Mo243 and Mo180 strongly expressed S100A9, CD169, and CD36. To assess the phenotypic changes in monocytes during SARS-CoV2 infection, we determined the frequencies of these metaclusters in each patient at admission and performed hierarchical clustering on these values (Fig. 2B). The upper branch of the hierarchical clustering included 20 COVID^{pos} (10 ARDS^{neg} and 10 ARDS^{pos}) and 1 COVID^{neg}ARDS^{pos} patient whereas the lower branch included 10 COVID^{pos} (7 ARDS^{neg} and 3 ARDS^{pos}) and 11 COVID^{neg}ARDS^{pos} (chi-square = 0.001) (Fig. 2B). We then analyzed the abundance of individual metaclusters and identified only 4 metaclusters out of 15 as differentially represented between the 3 groups of patients (Fig. 2C and Fig. S2). In particular, within ARDS^{pos} patients, Mo11 and M181 were less abundant in COVID-19^{pos} patients ($P < 0.01$ and $P < 0.05$, respectively), while Mo243 and Mo180 were more abundant ($P < 0.05$ and $P < 0.001$) (Fig. 2C). No differences were detected within COVID-19^{pos} groups (ARDS^{pos} versus ARDS^{neg}) (Fig. 2C). Interestingly, Mo243 and Mo180 were both enriched in cells highly expressing CD169, CD64, CD36, and CD14 (Fig. 2A and 2D). Additionally, Mo22 was present only in some COVID^{pos} patients and also expressed CD169 (Fig. 2B). Taken together, Mo243, Mo180, and Mo22 metaclusters were highly enriched in COVID-19^{pos} patients when compared to COVID-19^{neg} patients ($P < 0.0001$), with no difference regarding the ARDS status (Fig. 2E). Accordingly, CD169 was differentially expressed in COVID-19^{pos} versus COVID-19^{neg} patients ($P < 0.001$) (Fig. 2E). Altogether, our study including COVID-19 and non-COVID-19 critically ill patients suggest a specificity of

CD169 expression in COVID-19 patients, and greatly extend previous scRNAseq data showing an expansion of CD169-expressing monocytes in COVID-19 patients compared to healthy donors (Fig. 2F).[15,25,38–40] We then performed the FlowSOM analysis on cohort 2 and validated the enrichment of Mo243 and Mo180 in COVID-19^{pos} samples (Fig. S3A, S3B), these metaclusters also presenting a trend for high CD169 expression (Fig. S3C).

Monocyte metacluster enrichment in COVID-19 is correlated with a specific increase of effector memory T cells and plasma cells

To define a more global immune pattern and the relationship between immune cells in the context of the SARS-CoV2 infection, we sought for correlation between frequencies of clusters of T-, NK-, B-, and plasma cells (n = 136 clusters from the lymphoid panel, Fig. S1) and the 4 monocyte metaclusters (Mo11, Mo181, Mo243, and Mo180) previously described. This analysis identified 70 clusters with significantly correlated variations ($P < 0.05$) (Fig. S2). To strengthen the relevance of these correlations, we restrained further analysis to the 29 strongest relationships ($R > 0.5$ or < -0.5 and $P < 0.01$) between Mo180 or Mo243 (the two metaclusters enriched in COVID-19 patients) and other immune cell subsets (Fig. 3A and Table S4). As expected, Mo180 and Mo243 metaclusters were correlated ($R = 0.93$). Moreover, they were positively correlated with 18 clusters of T (n = 6), NK (n = 10), and plasma cells (n = 2), and inversely correlated with 11 clusters of T (n = 9), and NK cells (n = 2) (Fig. 3A). Among positively correlated clusters, plasmo_183 and plasmo_198 similarly expressed CD38, CD44, and CD27, whereas plasmo_183 was high for Ki-67 and HLA-DR, corresponding to an early plasma cell phenotype (Fig. 3B). NK cells were all marked by CD7 and T-bet expression, NK_209 being CD8^{high}, and NK_241 and NK_197 displaying a Ki-67^{high} proliferating phenotype. The related T8_147 and T8_161 clusters exhibited a CD45RA^{high}CD45RO^{low}CCD7^{low}CD27^{low}Tbet^{high}CD38^{high} effector phenotype. Few

T4 clusters were positively correlated with Mo180 and Mo243, among them T4_106 displayed an effector memory proliferating phenotype (Ki-67^{high}CD45RA^{low}CCR7^{low}CD45RO^{high}CD27^{high} and CTLA4^{high}PD1^{high}). T4_25 was also marked by an effector memory phenotype (CD45RA^{low}CCR7^{low}CD45RO^{pos}) and displayed a CD27^{low}CD127^{pos}CCR6^{pos}CxCR3^{neg}CD161^{pos} Th17 profile (Fig. 3B). Conversely, some T4 clusters were inversely correlated with Mo_180 and Mo_243, in particular clusters T4_6, T4_20, and T4_34, all three corresponding to naïve cells (CD45RA^{high}CD45RO^{low}CCR7^{high}), and T4_59 expressing a Th2 phenotype (CCR4^{high}). We then compared the abundance of these 29 lymphoid clusters correlated with Mo180 and Mo243 and highlighted the 22 differentially represented lymphoid clusters between the three groups of patients ($P < 0.05$) (Fig. 3C and Fig. S2). Only 7 clusters of CD4 T cells, and 2 clusters of CD8 T cells were at lower abundance in COVID-19^{pos}ARDS^{pos} patients compared to COVID-19^{neg}ARDS^{pos} patients. As previously discussed, T4_6, T4_20, and T4_34 corresponded to naïve cells, whereas within the effector memory cells, T4_7 and T4_45 were CD127^{low}, T4_24, T8_99, and T8_113 were CD127^{high}, and T4_59 was CCR4^{high}. Conversely, 13 clusters were enriched in COVID-19^{pos}ARDS^{pos} compared to COVID-19^{neg}ARDS^{pos} including: i) CTLA4^{high}PD1^{high} effector memory activated CD4 Tcells (T4_106); ii) Tbet^{high} Th1-like CD8 effector phenotype (T8_146, T8_147, and T8_161); iii) cytotoxic mature CD16^{pos}CD56^{low}CD7^{pos}Tbet^{pos}CD127^{neg} NK cells (NK_209, NK_241, NK_242, and NK_244) with in particular proliferating Ki-67^{high} NK cells (NK_241); and iv) proliferating plasmablasts (plasmo_183) and mature plasma cells (plasmo_198) (Fig. 3B and Fig. 3C). Of note, no cluster was differentially expressed between COVID-19^{pos}ARDS^{pos} and COVID-19^{pos}ARDS^{neg} groups (Fig. 3C and Fig. S2). Then, to explore the whole immune profile and define relationship with groups of patients, we performed correspondence analysis (CA) using, as a variable, the abundance of the myeloid (n = 4) and the lymphoid (n = 22) clusters differentially expressed between groups of patients (Fig. 3D). CA was developed to analyze frequency tables and visualize similarities between patients and co-occurrence of cell subsets.[41] The first and second dimension of the correspondence analysis explained 80.5 % and 13.5 % of the difference, respectively (Fig. 3D). The top-ten cell populations accounting for the difference between COVID^{pos} and COVID^{neg} patients were Mo243, Mo180, T8_146, NK_244, and T8_161 being increased and Mo181, T4_6, Mo11, T8_99, and T4_45 being decreased in COVID^{pos}. Altogether, these subsets corresponded to an increase in inflammatory monocytes (CD169^{high} CD64^{high}), Tbet^{high} Th1-like CD8 T cells, and mature NK cells and a decrease in naïve T4 cells and effector memory T4 and T8 cells. Interestingly, only the first dimension of the correspondence analysis segregated COVID-19^{pos}ARDS^{pos} from COVID-19^{neg}ARDS^{pos} ($P < 0.001$) and no statistical differences was found between COVID-19^{pos}ARDS^{pos} and COVID-19^{pos}ARDS^{neg} (Fig. 3D).

Evolution of immune cell clusters between D0 and D7 in COVID-19 patients defines high-risk clinical grade

We performed mass cytometry analysis for 21 patients at day 7 of hospitalization, including 7 COVID-19^{neg}ARDS^{pos}, 8 COVID-19^{pos}ARDS^{pos}, and 6 COVID^{pos}ARDS^{neg} patients, in order to follow up the kinetic of PBMC phenotypic alterations. The 42 samples (21 at day 0 and 21 at day 7) were parsed by correspondence analysis using, as a variable, the abundance of myeloid and lymphoid clusters (Fig. 4A). The first and second dimensions of the correspondence analysis explained 85.1 % and 9 % of the differences acquired between D0 and D7. The first dimension captured the difference between D0 and D7 only for COVID-19^{pos}ARDS^{pos} ($P < 0.01$) (Fig. 4A). Because of the limited number of samples, only a trend was observed for COVID^{pos}ARDS^{neg} ($P = 0.062$). The top-five enriched populations accounting for the differences between D0 and D7 for COVID-19^{pos}ARDS^{pos} patients were Mo11, Mo181, T8_113, T4_34, and NK_197, corresponding to an enrichment in non-classical monocytes ($CD14^{low}CD16^{high}CD64^{low}CD36^{low}S100A9^{high}$), in M-MDSC-like ($HLA\text{-}DR^{low}S100A9^{high}$), in effector memory $CD127^{high}$ T8 cells, in T4 naïve cells, and in $Ki\text{-}67^{high}$ proliferating NK cells. These 5 cell subsets were integrated in an immune score combining their fold change between D0 and D7. To define the relevance of this immune score in discriminating COVID-19 patients with unfavorable prognosis, we built a clinical score as the sum of events occurring during ICU stay (thromboembolic, ICU-acquired infection, septic shock, renal failure, and deaths) (Table 1). Interestingly, both the clinical and the immune scores were found correlated in severe COVID-19 patients, irrespectively of their ARDS status (Spearman $R = 0.71$; $P = 0.006$) (Fig. 4B). Finally, we analyzed changes between D0 and D7 of genes involved in IFN pathway. We found and upregulation of *IFNAR1* and *IFNAR2* during time in $COVID^{pos}ARDS^{pos}$ (Fig. S5A). Conversely, evolution of IFN type I target genes (*ISG15, IFI27, IFI44L, RSAD2*, and *IFIT1)* revealed a specific downregulation in $COVID^{pos}ARDS^{pos}$ samples. Interestingly, both IFNAR score and type I IFN score, obtained by combining the expression of IFN receptors and targets, respectively, presented a trend of correlation with the immune score (Fig. S5B), and the type I IFN score was significantly correlated with the CD169 expression (Fig. S5C).

Discussion

Immune response to COVID-19 infection has been recently intensively studied at both transcriptomic and proteomic levels. However, most studies focused on either the lymphoid[19,22,24] or the myeloid compartments,[12,21,23] and only few performed a wide analysis of the circulating immune landscape,[13,16,25,42,43] thus precluding the definition of complex patterns of immune parameter alterations associated with COVID-19 severity or physiopathology. Moreover, these studies were designed to identify differences in immune cell subsets frequencies between

COVID-19 patients and healthy donors, and eventually correlated with the severity of the disease, but did not include severe non-COVID-19 patients as controls, although critically ill patients were previously largely demonstrated to display immune reprogramming.[44] ARDS is a major adverse event occurring during ICU stay, leading to an overall mortality rate of 40 % to 60 %. Whether COVID-19 associated ARDS is clinically and biologically similar to other causes of ARDS remains controversial.[45,46] To address this point, we characterized for the first time, by mass cytometry, the immune landscape in COVID-19-associated ARDS compared to other causes of ARDS. We demonstrated that an increase of CD169^{pos} monocytes, correlated with specific changes of T, plasma, and NK cell subsets, defines COVID-19-associated ARDS and is not found in bacteria-associated ARDS, suggesting a COVID-19 specific immune reprogramming.

The amplification of CD169^{pos} circulating monocytes has already been highlighted in the context of COVID-19,[15,23,38,47] and is reminiscent of other inflammatory conditions found in viral infections, such as with Human Immunodeficiency Virus or Epstein-Barr Virus, in which the CD169 sialoadhesin is induced in an IFN-dependent manner on the surface of circulating monocytes.[48,49] Consistent with the inflammatory response, we showed that the accumulation of CD169^{pos} monocytes in COVID-19^{pos} patients is positively correlated with an increase of plasmablasts and mature plasma cells, Th1-like CD8 effector T cells, cytotoxic mature NK cells, and activated CD4 effector memory T cells displaying a CTLA4^{high}PD1^{high} phenotype. CD169^{pos} activated monocytes were detected in mild disease,[23] and were proposed to rise rapidly and transiently in patients with COVID-19, in association with a high expression of IFNγ and CCL8.[15] This could be due to the transient nature of this monocytic population, either losing CD169, being short-lived, or being recruited into tissues as CD169^{pos} macrophages, as suggested by the high expression of CCR2 on Mo243 and Mo180, the two monocyte subsets identified here in COVID-19 patients, and the local inflammation and lung tissue destruction mediated by monocyte-derived macrophages in severe cases of SARS-CoV2 infections.[50,51] Interestingly, we also found an upregulation of cytoplasmic S100A9 in monocyte subsets specifically amplified in COVID-19 patients irrespectively of their ARDS status. These data suggest that, in the early stage of the disease, monocytes could contribute to the burst of circulating calprotectin (S100A8/S100A9), recently proposed to contribute to the secondary cytokine release syndrome described in severe COVID-19 and attributed to neutrophils.[21] Despite phenotypic alterations, our data revealed a specific alteration of the response to type I IFN in COVID-19^{pos} *versus* COVD-19^{neg} ARDS patients after short stay in ICU, with an upregulation of IFN receptors without induction of IFN target genes. These results are reminiscent of the demonstration that deficiency of type I IFN pathway is associated with poor outcome in COVID-19 patients.[52,53]

Whereas a seroconversion score was recently associated with huge modifications immune parameters reflecting B, T, and NK cell function in non-ICU COVID patients,[54] our ICU patients clearly stand at a later stage of the disease, with 22 out of 29 already carrying neutralizing antibodies at D0. It is thus highly unlikely that the differential evolution of monocytic markers identified between D0 and D7 in our study could be attributable to seroconversion.

Within severe COVID-19 patients, we detected no significant differences between ARDS^{pos} and ARDS^{neg} immune profiles, indicating a specificity of the phenotype induced by SARS-CoV2 infection, irrespectively of the respiratory complications. While most published studies showed differences between mild and severe COVID-19 diseases, some of their conclusions might be obscured by the fact that ARDS by itself, mechanical ventilation, and/or nonspecific treatments might impact immune parameters.[55] A strength of our study comparing two groups of severe COVID-19 patients with or without ARDS is to highlight features directly related to the viral infection rather than to its respiratory complications or their treatment. Importantly, our cohort was homogeneous regarding treatment with in particular no immunosuppressive therapy at the time of sampling.

The small size of our cohort did not allow us to pinpoint a mortality prognostic factor based on our phenotypic data. However, we identified a specific immune pattern associated with the occurrence of the major adverse clinical events (thrombosis, nosocomial infection, septic shock, acute renal failure, and death) described in COVID-19 and combined as a clinical score. In particular, an increase of non-classical $CD14^{low}CD16^{pos}$ monocytes (Mo11), and $CD14^{pos}$HLA-DR^{low} M-MDSC-like (Mo181), both not expressing CD169, are markers of adverse events. This suggests that besides the early increase of $CD169^{pos}$ monocytes in all COVID-19 patients associated with T-cell dysfunctions, the immunological response to SARS-CoV2 infection features multiple alterations of monocytic subsets reflecting the severity of the disease. Consistent with these data, it was shown that $CD14^{pos}$HLA-DR^{low} cells were increased in critical COVID-19 patients,[21,26,56–58] while $CD14^{low}CD16^{pos}$ monocytes, able to migrate to the lung, were correlated with the length of stay in ICU.[15,23,59] Altogether, our study correlates the accumulation of non-classical monocytes and M-MDSCs occurring during the first days of ICU to adverse events.

Limitations of Study

Besides the low number of included patients, our study has some limitations. By focusing on severe patients with and without ARDS, we cannot make conclusions about phenotypic changes in mild and moderate diseases. The analysis would also benefit from comparison with other virus-associated ARDS. We thus analyzed a published dataset of flu-like illness and COVID patients, analyzed by mass cytometry.[21] Interestingly, by using CellCnn, we were able to define a filter that accurately discriminate flu-like illness from COVID samples, suggesting immune differences between both diseases (Fig. S4). Moreover, since the mass cytometry was conducted on PBMCs, we lack information on the neutrophil lineage, which appears affected in COVID-19 disease.[21] It would also be interesting to link these data with *in situ* data from lung tissue samples and bronchoalveolar lavages. Unfortunately, at the time of the study, bronchoalveolar fluid collection was not allowed in our institution for patients positive for SARS-CoV2. However, our detailed analysis of circulating immune cells shows that immune monitoring of severe COVID-19 patients brings interesting prognostic biomarkers independently of their clinical classification in $ARDS^{pos}$ versus $ARDS^{neg}$. Moreover, we demonstrated that at the biological level, COVID-19 associated ARDS is different from other causes of ARDS, and might benefit from personalized therapy in addition to standard ARDS management.[23,60]

Acknowledgments: We thank all donors, families, and surrogates, as well as the medical personnel in charge of patient care. We thank Catherine Blanc and Aurelien Corneau, from the CyPS core facility at Sorbonne University, Paris for access to the Helios mass cytometer. **Funding:** This work was supported by the University hospital of Rennes, CFTR² (COVID-19 Fast Track Recherche Rennes) grant (to F.R.) and by the Fondation pour la Recherche Médicale (FRM) and the Agence Nationale de la Recherche (ANR), Flash Covid-19 joint grant (HARMONICOV to M.Cog.).

Author contributions: Conceptualization, M.R., F.R., M.Le, J.M.T., M.Cog., and K.T.; Methodology, M.R., S.L.G, J.D., and K.T; Formal analysis, M.R., J.Fer., S.L., and S.C.; Investigation, S.L.G., J.D., C.M., M.G., N.B., C.V., M.La., I.B., and M.Cor.; Resources, F.R., M.Le., B.S, S.P., J.Feu., R.J., T.D.,V.K.T., and J.M.T.; Data curation, M.R., J.Fer. and F.R.; Writing - original draft preparation, M.R. and J.Fer.; Writing - review and editing, M.R., J.Fer., S.L.G., S.C., V.K.T., J.M.T., M.Cog., and K.T.; Visualization, M.R. and J.Fer.; Supervision, M.R. and K.T.; Project administration, M.R. and K.T.; Funding acquisition, F.R. and M.Cog.

Competing interests: J.Fer., F.R., S.L.G., J.D., M.Le., M.G., N.B., C.V., M.La., I.B., M.Cor., A.V., C.M., B.S., S.L., S.P., J.Feu., R.J., T.D., and M. Cog. declare no competing interest. M.R., S.C., V.K.T., J.M.T., and K.T. are the inventors of a patent EP 20305642.9 “A method for early detection of propensity to severe clinical manifestations Methods” submitted June 11th 2020 under University hospital of Rennes and Scailyte AG names.

Fig. 1: SARS-CoV2 induces specific phenotype of circulating immune cells

CellCnn analysis performed on single cells from myeloid (top) and lymphoid (bottom) panels on 39 samples at admission (Day 0) (COVID-19^{neg} [n = 9] and COVID-19^{pos} [n = 30]). **(A)** Frequencies of cells discovered by the best-performing CellCnn filter in COVID-19^{neg} (blue) and COVID-19^{pos} (orange) patients for each panel. Mann-Whitney tests, ****P < 0.0001. **(B)** Cells defined by the best-performing CellCnn filters enrichment shown on tSNE and representative markers for each panel (CD14 and CD38 [see additional markers in Fig. S2]).

Fig. 2: CD169 monocytes are enriched in SARS-CoV2 infected patients

(A) Heatmap of the 15 monocyte metaclusters defined after FlowSOM analysis. **(B)** Relative abundance of metaclusters among monocytes for each patient and hierarchical clustering of COVID-19^{neg}ARDS^{pos} (n=12, green), COVID-19^{pos}ARDS^{pos} (n=13, blue), and COVID-19^{pos}ARDS^{neg} (n=17, red). **(C)** Abundance of metaclusters differentially expressed between groups, among singlet cell analyzed. **(D)** Expression of the corresponding markers (mean metal intensity) for background (gray), Mo11 and Mo181 (orange), and Mo243 and Mo180 (blue) metaclusters. **(E)** Abundance of Mo22, Mo180, and Mo243 and expression of CD169 (Box and Whiskers with 10 and 90 percentile). **(F)** UMAP from scRNAseq of COVID-19 patients (COVID-19) and healthy donors (healthy) highlighting CD14 and CD169 expression (data obtained from Wilk et al.[25]) Kruskal-Wallis test with Dunn’s multiple comparison correction, *P < 0.05, **P < 0.01, ***P < 0.001.

Fig.3: Monocyte metaclusters enriched in COVID-19 are correlated with effector memory T cells and plasma cells

(A) Correlation between Mo180 and Mo243 and lymphoid clusters (see heatmap for all lymphoid clusters and markers in Fig. S2) from all patients at D0 (COVID-19^{neg}ARDS^{pos} [n=12], COVID-19^{pos}ARDS^{pos} [n=13], and COVID-19^{pos}ARDS^{neg} [n=17]. Only strong correlations (Spearman R > 0.5 or R < -0.5 and P < 0.01) are shown (see all significant correlations [P < 0.05] in Fig. S2 and Table S4). **(B)** Heatmap showing marker expression for the lymphoid clusters (Spearman R > 0.5 or R < -0.5 and P < 0.001) strongly correlated with Mo180 and Mo243 (see heatmap for all clusters and markers in Fig. S2). **(C)** Abundance of lymphoid clusters differentially expressed between groups, among singlet cells analyzed. Kruskal-Wallis test with Dunn's multiple comparison correction, *P < 0.05, **P < 0.01, ***P < 0.001 [see all clusters in Fig. S2]). **(D)** Two first dimensions of correspondence analysis accounting for 84 % of the association between immune clusters differentially expressed between groups (n= 4 monocyte- and n=22 lymphoid-clusters), and patients. For clarity, patients and immune cells are shown on 2 different plots. Dimensions 1 and 2 coordinates are compared between groups of patients. Kruskal-Wallis test with Dunn's multiple comparison correction, ****P < 0.0001.

Fig. 4: Evolution of immune cell subsets between D0 and D7, defines high-risk clinical grade COVID-19 patients

(A) Two first dimension of correspondence analysis accounting for 94.1% of the association between immune clusters differentially expressed between groups (n= 4 monocyte and n=22 lymphoid clusters), and patients for which a follow-up of 7 days was available (COVID-19^{neg}ARDS^{pos} [n=7], COVID-19^{pos}ARDS^{pos} [n=8], and COVID-19^{pos}ARDS^{neg} [n=6]). For clarity, patients and immune cells are shown on 2 different plots. Dimensions 1 and 2 coordinates were compared between D0 and D7 for each group of patients. Wilcoxon matched-pairs signed rank tests, **P < 0.01. **(B)** Spearman correlation between immune and clinical score for COVID-19^{pos} patients (ARDS^{pos} [n=8] and ARDS^{neg} [n=6]).

Table 1: Patients' characteristics for the cohort 1

	COVID-19^{neg} ARDS^{pos}	COVID-19^{pos} ARDS^{pos}	COVID-19^{pos} ARDS^{neg}
Patients D0/D7, n	12/7	13/8	17/6
Age, median (IQR)	62 (48.2-66.7)	59 (53.5-67.5)	55 (46-67)
Male, n (%)	7 (58)	10 (77)	12 (71)
ICU/Clinical ward, n	12/0	13/0	11/6*
SAPS II, median (IQR)	44.5 (29.2-59.2)	33 (19.5-39.5)	22 (13-28)*
Length of stay in ICU, median (IQR)	11.5 (4.5-18.7)	15 (11-54)	2 (1-2)**
Length of stay in Hospital, median (IQR)	18 (7-30.5)	22 (15-62.5)	9 (7.5-13)
Comorbidities			
BMI, median (IQR)	26.4 (19.5-28.4)	28.6 (25-32)	28.1 (22.3-32.1)
Chronic cardiovascular disease, n (%)	1 (8.3)	3 (23)	1 (5.8)
Diabetes, n (%)	2 (16.7)	3 (23)	1 (5.8)
Chronic respiratory disease, n (%)	1 (8.3)	0 (0)	0 (0)
Chronic kidney disease, n (%)	0 (0)	2 (15.4)	0 (0)
Cancer, n (%)	3 (25)	0 (0)	0 (0)
Severity criteria			
Maximal O_2 (L/min), median (IQR)	10 (7.5-15)	14 (9.2-15)	3 (2-5)
Invasive ventilation, n (%)	12 (100)	13 (100)	0 (0)
PaO_2/FiO_2, median (IQR)	116.5 (75.2-161.9)	106 (95.5-240)	313 (218.5-340.3)
Events occurring during follow up			
Thromboembolic, n (%)	4 (33.3)	4 (30.8)	1 (5.8)
ICU-acquired infections, n (%)	2 (16.7)	7 (53.8)	0 (0)
Septic shock, n (%)	3 (25)	2 (15.4)	0 (0)
Renal failure, n (%)	5 (41.7)	8 (61.5)	0 (0)
Deaths, n (%)	4 (33.3)	1 (7.7)	0 (0)

*: all patients except 1 required O_2 at > 2 L/mn at admission; **: For patients in ICU; n: number; IQR: interquartile range; SAPS II: simplified acute physiology score

STAR*METHODS

KEY RESOURCES TABLE

REAGENT or RESOURCE	SOURCE	IDENTIFIER
Antibodies		
CD11c (3.9), Purified	BioLegend	Cat# 301602, RRID:AB_314172
CD33 (WM53), Purified	BioLegend	Cat# 303402, RRID:AB_314346
CD209 (9E9A8), Purified	BioLegend	Cat# 330102, RRID:AB_1134253
CD14 (M5E2), Purified	BioLegend	Cat# 301802, RRID:AB_314184
CD123 (6H6), Purified	BioLegend	Cat# 306002, RRID:AB_314576
CD21 (Bu32), Purified	BioLegend	Cat# 354902, RRID:AB_11219188
CD192 (K036C2), Purified	BioLegend	Cat# 357202, RRID:AB_2561851
CD163 (GHI/61), Purified	BioLegend	Cat# 333602, RRID:AB_1088991
CD36 (5-271), Purified	BioLegend	Cat# 336202, RRID:AB_1279228
CD86 (IT2.2), Purified	BioLegend	Cat# 305402, RRID:AB_314522
CD169 (7-239), Purified	BioLegend	Cat# 346002, RRID:AB_2189031
CD274 (29E.2A3), Purified	BioLegend	Cat# 329719, RRID:AB_2565429
CD254 (MIH24), Purified	BioLegend	Cat# 347501, RRID:AB_2044062
CD106 (EPR5047), Purified	Abcam	Cat# ab134047, RRID:AB_2721053
CD3 (UCHT1), Purified	BioLegend	Cat# 300402, RRID:AB_314056
CD49a (TS2/7), Purified	BioLegend	Cat# 328302, RRID:AB_1236385
gp38 (REA446), Purified	Miltenyi Biotec	Cat# 130-107-017, RRID:AB_2653261
CD80 (2D10), Purified	BioLegend	Cat# 305202, RRID:AB_314498
CD34 (581), Purified	BioLegend	Cat# 343502, RRID:AB_1731898
CD1a (HI149), Purified	BioLegend	Cat# 300102, RRID:AB_314016
CX3CR1 (2A9-1), Purified	BioLegend	Cat# 341602, RRID:AB_1595422
CD32 (FUN-2), Purified	BioLegend	Cat# 303202, RRID:AB_314334
CD54 (HA58), Purified	BioLegend	Cat# 353102, RRID:AB_11204426
CD195 (J418F1), Purified	BioLegend	Cat# 359102, RRID:AB_2562457
CD206 (15-2), Purified	BioLegend	Cat# 321102, RRID:AB_571923
S100A9 (A15105J), Purified	BioLegend	Cat# 600302, RRID:AB_2721747

CD45RA (HI100), Purified	BioLegend	Cat# 304102, RRID:AB_314406
CD172a (15-414), Purified	BioLegend	Cat# 372102, RRID:AB_2629807
CD68 (Y1/82A), Purified	BioLegend	Cat# 333802, RRID:AB_1089058
CD11b (ICRF44), 209Bi	Fluidigm	Cat# 3209003, RRID:AB_2687654
CD8a (RPA-T8), Purified	BioLegend	Cat# 301053, RRID:AB_2562810
CD4 (RPA-T4), Purified	BioLegend	Cat# 300502, RRID:AB_314070
CD25 (BC96), Purified	BioLegend	Cat# 302602, RRID:AB_314272
CD38 (HIT2), Purified	BioLegend	Cat# 303502, RRID:AB_314354
CXCR3 (G025H7), Purified	BioLegend	Cat# 353733, RRID:AB_2563724
FoxP3 (259D/C7), Purified	BD Biosciences	Cat# 560044, RRID:AB_1645589
CD7 (CD7-6B7), Purified	BioLegend	Cat# 343111, RRID:AB_2563761
Gata-3 (TWAJ), Purified	Thermo Fisher Scientific	Cat# 14-9966-82, RRID:AB_1210519
CCR7 (G043H7), Purified	BioLegend	Cat# 353237, RRID:AB_2563726
CCR6 (G034E3), Purified	BioLegend	Cat# 353427, RRID:AB_2563725
CD27 (O323), Purified	BioLegend	Cat# 302802, RRID:AB_314294
CD10 (HI10a), Purified	BioLegend	Cat# 312223, RRID:AB_2562828
CD117 (104D2), Purified	BioLegend	Cat# 105814, RRID:AB_313223
CCR4 (L291H4), Purified	BioLegend	Cat# 359402, RRID:AB_2562364
CD161 (HP-3G10), Purified	BioLegend	Cat# 339919, RRID:AB_2562836
CD185 (J252D4), Purified	BioLegend	Cat# 356902, RRID:AB_2561811
RORgt (AFKJS-9), Purified	Thermo Fisher Scientific	Cat# 14-6988-82, RRID:AB_1834475
CD294 (BM16), Purified	BioLegend	Cat# 350102, RRID:AB_10639863
LAG-3 (7H2C65), Purified	BioLegend	Cat# 369202, RRID:AB_2616877
CTLA-4 (L3D10), Purified	BioLegend	Cat# 349902, RRID:AB_10642827
PD-1 (EH12.2H7), Purified	BioLegend	Cat# 329941, RRID:AB_2563734
Tim-3 (F38-2E2), Purified	BioLegend	Cat# 345019, RRID:AB_2563790
CD127 (A019D5), Purified	BioLegend	Cat# 351337, RRID:AB_2563715
Bcl-6 (k112-91), Purified	BD Biosciences	Cat# 561520,

		RRID:AB_10713172
T-bet (4B10), Purified	BioLegend	Cat# 644825, RRID:AB_2563788
CD45RO (UCHL1), Purified	BioLegend	Cat# 304239, RRID:AB_2563752
CD56 (HCD56), Purified	BioLegend	Cat# 318302, RRID:AB_604092
Ki-67 (Ki-67), Purified	BioLegend	Cat# 350523, RRID:AB_2562838
CD44 (BJ18), Purified	BioLegend	Cat# 338802, RRID:AB_1501199
CD45 (HI30), 89Y	Fluidigm	Cat# 3089003, RRID:AB_2661851
CD326 (9C4), Purified	BioLegend	Cat# 324229, RRID:AB_2563742
CD19 (HIB19), Purified	BioLegend	Cat# 302202, RRID:AB_314232
HLA-DR (10.1), Purified	BioLegend	Cat# 307602, RRID:AB_314680
CD31 (WM59), Purified	BioLegend	Cat# 303127, RRID:AB_2563740
CD16 (B73.1), Purified	BioLegend	Cat# 360702, RRID:AB_2562693
CD64 (L243), Purified	BioLegend	Cat# 305029, RRID:AB_2563759
Biological Samples		
Chemicals, Peptides, and Recombinant Proteins		
EQ Four Element Calibration Beads	Fluidigm	Cat# 201078
Antibody Stabilizer PBS	Candor Bioscience	Cat# 131050
Bond-Breaker™ TCEP Solution	Thermo Fisher Scientific	Cat# 77720
Cell-ID™ Intercalator-Ir	Fluidigm	Cat# 201192B
Cell-ID™ Cisplatin-198Pt	Fluidigm	Cat# 201198
Cell Acquisition Solution	Fluidigm	Cat# 201240
Critical Commercial Assays		
Transcription factor staining buffer set	Miltenyi Biotec	Cat# 130-122-981
Maxpar® X8 Multimetal Antibody Labeling Kit	Fluidigm	Cat# 201300
Preamp Master Mix	Fluidigm	Cat# 100-5580
Reverse Transcription Master Mix	Fluidigm	Cat# 100-6298
TaqMan Universal PCR Master Mix (2X)	Life Technologies	Cat# PN 4304437
96.96 DNA Binding Dye Sample/Loading Kit—10 IFCs	Fluidigm	Cat# BMK-M10-96.96-EG
Deposited Data		
CyTOF data	Chevrier et al, Cell Reports Medicine, 2021	DOI: 10.1016/j.xcrm.2020.100166

scRNAseq sata	Wilk et al, Nat Med, 2020	DOI: 10.1038/s41591-020-0944-y
CyTOF data	Schulte-Schrepping et al, Cell, 2020	DOI: 10.1016/j.cell.2020.08.001
CyTOF data	This paper	DOI: 10.17632/xg9k72r5rt.1
CyTOF data	This paper	DOI: 10.17632/c29frc3y6s.1
Clinical data	This paper	DOI: 10.17632/5n8df8jvk4.1
Oligonucleotides		
IFIT1: interferon induced protein with tetratricopeptide repeats 1	TaqMan® Assays, ThermoFisher Scientific	Hs03027069_s1
IFNAR1: interferon alpha and beta receptor subunit 1	TaqMan® Assays, ThermoFisher ScientificThermoFisher Scientific	Hs01066116_m1
ISG15: ISG15 ubiquitin-like modifier	TaqMan® Assays, ThermoFisher ScientificThermoFisher Scientific	Hs01921425_s1
IFI27: interferon alpha inducible protein 27	TaqMan® Assays, ThermoFisher Scientific	Hs01086373_g1
IFI44L: interferon induced protein 44 like	TaqMan® Assays, ThermoFisher Scientific	Hs00915287_m1
RSAD2: radical S-adenosyl methionine domain containing 2	TaqMan® Assays, ThermoFisher Scientific	Hs00369813_m1
IFNAR2: interferon alpha and beta receptor subunit 2	TaqMan® Assays, ThermoFisher Scientific	Hs01022059_m1
ELF1: E74-like factor 1 (ets domain transcription factor)	TaqMan® Assays, ThermoFisher Scientific	Hs00152844_m1
Software and Algorithms		
CellCnn, ScaiVision platform	Scailyte AG	version 0.3.6
R	https://www.cran.r-project.org	v3.6.3
Premessa (R package)	https://github.com/ParkerICI/premessa	premessa 0.2.6
viSNE (Cytobank)	Amir et al,Nat Biotechnol (2014)	NA
FlowSOM (Cytobank)	Van Gassen et al, Cytometry A (2015)	NA
Rstudio	https://rstudio.com/	v1.2.5033
pheatmap (R package)	https://cran.r-project.org/package=pheatmap	v1.0.12 (CRAN)
Cytobank	Kotecha et al., 2010 https://www.cytobank.org	https://doi.org/10.1002/0471142956.cy1017s53
Kaluza	Beckman Coulter	v2.1.00002
Prism (software)	https://www.graphpad.com	v8

RESOURCE AVAILABILITY

Lead contact

Further information and requests for resources and reagents should be directed to and will be fulfilled by the Lead Contact, Mikael Roussel (mikael.roussel@chu-rennes.fr)

Material Availability

The study did not generate new unique reagents.

Data and Code Availability

Additional Supplemental Items are available from Mendeley Data at http://dx.doi.org/10.17632/xg9k72r5rt.1, http://dx.doi.org/10.17632/c29frc3y6s.1, and http://dx.doi.org/10.17632/5n8df8jvk4.1

EXPERIMENTAL MODEL AND SUBJECT DETAILS

Patients

This study was performed in the infectious diseases department and intensive care unit (ICU) at Rennes University Hospital. The study design was approved by our ethic committee (CHU Rennes, n°35RC20_9795_HARMONICOV, ClinicalTrials.gov Identifier: NCT04373200) and informed consent was obtained from patients in accordance with the Declaration of Helsinki. Patients with malignancy, HIV-infected patients, and patients with preexisting immune disorders or receiving immunosuppressive agents were excluded. The presence of SARS-CoV-2 in respiratory specimens (nasal and pharyngeal swabs or sputum) was detected by real-time reverse transcription polymerase chain reaction (RT-PCR) methods (TaqPath COVID-19, ThermoFisher).

Cohort 1: Peripheral blood was collected in tubes containing lithium heparin from COVID-19^{neg}ARDS^{pos}, COVID-19^{pos}ARDS^{pos}, and COVID-19^{pos}ARDS^{neg} patients. Peripheral blood samples were drawn at D0 and D7. PBMC were isolated from whole blood using ficoll before cryopreservation. All patients provided written informed consent. The following data were recorded: gender, age, preexisting chronic kidney disease and acute kidney failure during the ICU stay,[61] preexisting chronic heart failure,[62] Body Mass Index (BMI), SAPS II at admission,[63] duration of mechanical ventilation, length of hospital stay, and outcome (alive or dead) on day 7, day 30 and day 90. The occurrence of nosocomial infection, defined following CDC criteria as previously described,[64] was also recorded during hospital stay. For each patient, a clinical score was built to summarize the occurrence of adverse clinical events frequently encountered during hospitalization.[64,65] Each of the following events: thromboembolic events, nosocomial infection, septic shock, acute renal failure, and death counting as one point, the score varies from 0 (no adverse events) to 5. Patients' characteristics for cohort 1 are reported in Table 1 and Table S1.

Cohort 2: Same inclusion criteria were applied to cohort 2. Only patients at D0 were included. Patients' characteristics for cohort 1 are reported in Table S1 and Table S2.

METHODS DETAILS

Mass cytometry analysis

PBMC from patients were thawed. Briefly, cells were stained 5 minutes in RPMI supplemented with 0.5 µM Cisplatin Cell-ID™ (Fluidigm, San Francisco, CA) in RPMI 1640 before washing with 10% FCS in RPMI 1640. Cell pellets were resuspended in 80µl of 0.5% BSA in PBS. Then 60 µl of each surface staining cocktail, lymphoid or myeloid, were added to 40µl of resuspended cells. After staining, cells were washed in 0.5% BSA in PBS before fixation/permeabilization with the transcription factor staining buffer set (Miltenyi, Bergisch-Gladbach, Germany). Then 60µl of each surface staining cocktail, lymphoid or myeloid, were added to 40µl of resuspended cells in Perm Buffer. The panel of antibodies is listed in Table S3 and in Key Resources Table. After intracellular staining, cells were washed twice before staining in DNA intercalator solution (2.5% Paraformaldehyde, 1:3200 Cell-ID™ Intercalator-Ir (Fluidigm, San Francisco, CA) in PBS). Samples were cryopreserved at -80°C until acquisition on Helios™ System (Fluidigm, San Francisco, CA).

Antibodies and reagents

Purified antibodies for mass cytometry were obtained in carrier/protein-free buffer and then coupled to lanthanide metals using the MaxPar antibody conjugation kit (Fluidigm Inc.) according to manufacturer's recommendations. Following the protein concentration determination by measurement of absorbance at 280 nm and titration on positive controls, the metal-labeled antibodies were diluted in Candor PBS Antibody Stabilization solution (Candor Bioscience, Germany) for long-term storage at 4°C. Antibodies used are listed in Table S3 and Key Resources Table.

Quantitative real-time polymerase chain reaction

Total RNA was extracted from PAXgene blood RNA kit (Qiagen, Valencia,CA) using a Hamilton Microlab STARlet Automated Handler (Atlantic Lab Equipment, Beverly, MA). cDNA was then prepared using Reverse Transcription Master Mix (Fluidigm Sunnyvale, CA) and gene expression preamplification was performed with Fluidigm Preamp Master Mix and Taqman Assays (Invitrogen, Thermo Fisher Scientific Inc, Carlsbad, CA, USA). After loading the reaction chambers using the integrated fluid circuit (IFC) HX controller from Fluidigm, the realtime PCR was performed in a BioMark HD system (Fluidigm Corp., USA) using single probe (FAM-MGB, reference: ROX) settings and GE 96x96 standard v1 protocol. Data processing took place using the Fluidigm real-time PCR analysis software (v. 4.1.3). For each sample, the cycle threshold (CT) value for the gene of interest was determined and normalized to the housekeeping gene *ELF1*. The relative level of expression of each gene for each patient at D7 compared to D0 was assessed using the 2-ddCT method. For all D0 samples, the relative level of expression of each gene was assessed by 2-dCT method Type I IFN response score was determined as Log2 of the mean of the following genes: *ISG15*, *IFI27*, *IFI44L*, *RSAD2* and *IFIT*. IFNAR score was considered as Log2 of the mean of the following genes: *IFNAR1* and *IFNAR2*.

Detection of SARS-CoV-2 neutralizing antibodies

The viral strain (RoBo strain), which was cultured on Vero-E6 cells (ATCC CRL-1586), used for the nAb assay was a clinical isolate obtained from a nasopharyngeal aspirate of a patient HOS at the University Hospital of Saint-Etienne for severe COVID-19. The strain was diluted in Dulbecco's modified Eagle's medium–2% fetal calf serum in aliquots containing 100–500 tissue culture infectious doses 50% (TCID50) per ml. Each serum specimen was diluted 1:10 and serial twofold dilutions were mixed with an equal volume (100 µL each) of virus. After gentle shaking for 30 min at room temperature, 150 µL of the mixture was transferred to 96-well microplates covered with Vero-E6 cells. The plates were then placed at 37°C in a 5% CO_2 incubator. Measurements were obtained microscopically 5–6 days later when the cytopathic effect of the virus control reached ~100 TCID50/150 µL. The serum was considered to have protected the cells if >50% of the cell layer was preserved. The neutralizing titer is expressed as the inverse of the higher serum dilution that protected the cells.

QUANTIFICATION AND STATISTICAL ANALYSIS

Mass Cytometry Preprocessing

After acquisition, intrafile signal drift was normalized and .fcs files were obtained using CyTOF software. To diminish batch effects, all files were normalized on EQ Beads (Fluidigm Sciences) using the premessa R package (https://github.com/ParkerICI/premessa). Files were then uploaded to the Cytobank cloud-based platform (Cytobank, Inc.). Data were first arcsinh-transformed using a cofactor of 5. For all files, live single cells were selected by applying a gate on DNA1 vs. DNA2 followed by a gate on DNA1 vs. Cisplatin, then beads were removed by applying a gate on the beads channel (Ce140Di) vs. DNA.1 Normalized, transformed and gated values were exported as FCS files.

CellCnn analysis

Identification of a Covid-19-specific cell-identity signature was carried out using the CellCnn algorithm,[35] implemented in Pytorch in the ScaiVision platform (version 0.3.6, © Scailyte AG). Briefly, this is a supervised machine learning algorithm that trains a convolutional neural network with a single layer to predict sample-level labels using single-cell data as inputs. Data from each CyTOF panel was analyzed separately, in each case using all measured protein markers to train a series of CellCnn networks with varying hyperparameters. Each sample was given a label corresponding to the Covid-19 status of the patient from which the sample was drawn (positive or negative). To generate input data for training CellCnn, sub-samples of 2000 cells, termed multi-cell inputs (MCIs), were chosen randomly from each sample independently. For each training epoch, 2000 MCIs from each label class (Covid-19^{pos} or Covid-19^{neg}) were presented to the network in random order. During training, 30 % of the samples were set aside for validation, chosen in a stratified manner to maintain the relative proportions of each class. 50 independent networks were generated for each CyTOF panel using hyperparameters randomly chosen from the following options: i) number of filters: (2, 3, 5, 7, and 10), ii) top-k pooling percentage: (1, 5, 10, 20, and 30), iii) dropout probability: (0.3, 0.4, and 0.6), iv) learning rate: (0.001, 0.003, and 0.01), and v) weight decay: (0.00001, 0.0001, 0.001, 0.01, and 0.1). Training was performed with a batch size of 50. Adam was used as an optimizer {kingma2015adam}, with a beta1 coefficient of 0.999 and a beta2 coefficient of 0.99. Each network was trained for a maximum of 50 epochs, or until the validation loss no longer decreased for 10 consecutive epochs. At the end of training, the weights from the epoch with lowest validation loss were returned. Representative filters were determined by clustering the filters from all networks achieving $\geq$ 90 % accuracy on the validation samples, then choosing the filter in each cluster with the minimum distance to all other filters in that cluster. For both CyTOF panels, a single representative filter showing the largest positive association with the Covid-19^{pos} label class was used to calculate cell-level filter response scores. Thresholds were set on the filter response scores to select Covid-19-associated cells by calculating the relative frequencies of selected cells in each sample at 100 different thresholds for each filter, then performing a logistic regression to predict sample labels. For each threshold, the data was first split in a stratified manner into a training set, comprising 60 % of samples, and a test set, comprising 40 % of samples. The logistic regression was performed on the training set, and the accuracy of resulting predictions was calculated on the test set. This procedure was performed 10 times, with randomly chosen training/test splits, and the mean of the resulting accuracies for each threshold was calculated. For the lymphoid panel, one threshold (9.63) achieved the highest accuracy and was set as the final threshold. For the myeloid panel, multiple thresholds achieved the same level of accuracy; the lowest of these (4.96) was set as the final threshold. The relative frequencies of cells in each sample with filter response scores greater than or equal to the respective thresholds were calculated and compared using a Wilcoxon rank-sum test.

viSNE, FlowSOM, and hierarchical clustering

We first performed a dimension reduction for both panels (i.e. myeloid and lymphoid) and all cleaned-up 63 files were first analyzed using viSNE, based upon the Barnes–Hut implementation of t-SNE. Equal downsampling was performed, based on the lowest event count in all files (lymphoid panel) or on the maximum total events allowed by Cytobank (myeloid panel). For the myeloid panel, the following parameters were used: perplexity = 45; iterations = 5000; theta = 0.5; all 37 channels selected. For the lymphoid panel the parameters were as follows: perplexity = 45; iterations = 7500; theta = 0.5; all 36 channels selected.

Then we applied a clustering method using the FlowSOM clustering algorithm. FlowSOM uses Self-Organizing Maps (SOMs) to partition cells into clusters based on their phenotype, and then builds a Minimal Spanning Tree (MST) to connect the nodes of the SOM, allowing the identification of metaclusters (i.e. group of clusters). We performed the FlowSOM algorithm on the previous viSNE results, using all events and panel channels, and the following parameters: clustering method = hierarchical consensus, iterations = 10, number of clusters = 256, number of metaclusters = 30. For both panels, each metacluster (containing a given number of clusters) was manually annotated based on his marker expression phenotype, his projection on the viSNE and his localization in the FlowSOM MST.

We first analyzed the myeloid panel. Out of 30 metaclusters defined by the FlowSOM approach, we identified 13 metaclusters with monocyte markers, other metaclusters contained other cell types, low count of cells or remaining doublets or dead cells. We visually identified 2 (Mo18 and Mo26) out of the 13 metaclusters that were heterogeneous. These 2 metaclusters were manually split into 2 new metaclusters (identified respectively as Mo180, Mo181 and Mo214, Mo243) (Fig. S1B). Thus, altogether we analyzed 15 metaclusters of myeloid cells. Regarding the lymphoid compartment, we noticed that FlowSOM defined metaclusters at the lineage level, thus we retain all the 136 clusters included in 10 metaclusters of interest (i.e. containing lymphoid lineage markers) (Fig. S1C). All metaclusters and clusters phenotypes including their abundances and mean marker intensity were then exported from Cytobank for further analyses. Cytometry data was explored with Kaluza Analysis Software (Beckman Coulter). Hierarchical clustering and heatmaps were generated with R v3.6.3, using Rstudio v1.2.5033 and the pheatmap package.

Statistical analysis

Statistical analyses were performed with Graphpad Prism 8.4.3. P values were defined by a Kruskal-Wallis test followed by a Dunn's post-test for multiple group comparisons or by Wilcoxon matched-pairs signed rank tests as appropriate. Correlations were calculated using Spearman test. * $P < 0.05$, ** $P < 0.01$, *** < 0.001, and **** $P < 0.0001$. Hierarchical clustering of the patients was performed using euclidean distance and complete clustering. Correspondence analysis was performed using the package factoshiny using as variable the abundance in cell subsets for each patient.

Supplementary Materials:

Figure S1. Description of the 2 cohorts of patients, CyTOF experimental design and data analysis pipeline. Related to Table 1 and Figures 1 and 2.

Figure S2. Supplemental data for cohort 1. Related to Figure 1B, 2 and 3.

Figure S3. CellCnn and FlowSOM analysis for cohort 2. Related to Figures 1, 2 and 3.

Figure S4. CellCnn analysis for Chevrier et al. (Cell Reports Medicine, 2021) data[1] and for Schulte- Schrepping et al. (Cell, 2020) data[2]. Related to Figure 1.

Figure S5. IFN I pathway. Related to Figure 4.

Table S1. Clinical data (excel spreadsheet). Related to Table 1.

Table S2. Patients' characteristics for the cohort 2. Related to Table 1.

Table S3. Panel of antibodies. Related to STAR Methods.

Table S4. Spearman correlation between myeloid and lymphoid clusters. Related to Figure 3.

References and Notes:

1 Williamson EJ, Walker AJ, Bhaskaran K, Bacon S, Bates C, Morton CE *et al.* Factors associated with COVID-19-related death using OpenSAFELY. *Nature* 2020; **584**: 430–436.

2 Guan W-J, Ni Z-Y, Hu Y, Liang W-H, Ou C-Q, He J-X *et al.* Clinical Characteristics of Coronavirus Disease 2019 in China. *The New England journal of medicine* 2020; **382**: 1708–1720.

3 Huang C, Wang Y, Li X, Ren L, Zhao J, Hu Y *et al.* Clinical features of patients infected with 2019 novel coronavirus in Wuhan, China. *Lancet* 2020; **395**: 497–506.

4 Sepsis) CTG (Clinical R in IC and STG for GE and R in, Helms J, Tacquard C, Severac F, Leonard-Lorant I, Ohana M *et al.* High risk of thrombosis in patients with severe SARS-CoV-2 infection: a multicenter prospective cohort study. *Intens Care Med* 2020; **46**: 1089–1098.

5 Schultze JL, Aschenbrenner AC. COVID-19 and the human innate immune system. *Cell* 2021. doi:10.1016/j.cell.2021.02.029.

6 Chen G, Wu D, Guo W, Cao Y, Huang D, Wang H *et al.* Clinical and immunologic features in severe and moderate Coronavirus Disease 2019. *J Clin Invest* 2020; **130**: 2620–2629.

7 Jeannet R, Daix T, Formento R, Feuillard J, François B. Severe COVID-19 is associated with deep and sustained multifaceted cellular immunosuppression. *Intens Care Med* 2020; **46**: 1769–1771.

8 Libster R, Marc GP, Wappner D, Coviello S, Bianchi A, Braem V *et al.* Early High-Titer Plasma Therapy to Prevent Severe Covid-19 in Older Adults. *New Engl J Med* 2021; **384**: 610–618.

9 Arabi YM, Murthy S, Webb S. COVID-19: a novel coronavirus and a novel challenge for critical care. *Intens Care Med* 2020; **46**: 833–836.

10 Paassen J van, Vos JS, Hoekstra EM, Neumann KMI, Boot PC, Arbous SM. Corticosteroid use in COVID-19 patients: a systematic review and meta-analysis on clinical outcomes. *Crit Care* 2020; **24**: 696.

11 Ni Y-N, Chen G, Sun J, Liang B-M, Liang Z-A. The effect of corticosteroids on mortality of patients with influenza pneumonia: a systematic review and meta-analysis. *Crit Care* 2019; **23**: 99.

12 Agrati C, Sacchi A, Bordoni V, Cimini E, Notari S, Grassi G *et al.* Expansion of myeloid-derived suppressor cells in patients with severe coronavirus disease (COVID-19). *Cell Death Differ* 2020; **27**: 3196–3207.

13 Arunachalam PS, Wimmers F, Mok CKP, Perera RAPM, Scott M, Hagan T *et al.* Systems biological assessment of immunity to mild versus severe COVID-19 infection in humans. *Science* 2020; **369**: 1210–1220.

14 Chen Z, Wherry EJ. T cell responses in patients with COVID-19. *Nat Rev Immunol* 2020; **20**: 529–536.

15 Chevrier S, Zurbuchen Y, Cervia C, Adamo S, Raeber ME, Souza N de *et al.* A distinct innate immune signature marks progression from mild to severe COVID-19. *Cell Reports Medicine* 2021; **2**: 100166.

16 Hadjadj J, Yatim N, Barnabei L, Corneau A, Boussier J, Smith N *et al.* Impaired type I interferon activity and inflammatory responses in severe COVID-19 patients. *Science* 2020; **369**: 718–724.

17 Lucas C, Wong P, Klein J, Castro TBR, Silva J, Sundaram M *et al.* Longitudinal analyses reveal immunological misfiring in severe COVID-19. *Nature* 2020; **584**: 463–469.

18 Mann ER, Menon M, Knight SB, Konkel JE, Jagger C, Shaw TN *et al.* Longitudinal immune profiling reveals key myeloid signatures associated with COVID-19. *Sci Immunol* 2020; **5**: eabd6197.

19 Mathew D, Giles JR, Baxter AE, Oldridge DA, Greenplate AR, Wu JE *et al.* Deep immune profiling of COVID-19 patients reveals distinct immunotypes with therapeutic implications. *Science* 2020; **369**: eabc8511.

20 Ren X, Wen W, Fan X, Hou W, Su B, Cai P *et al.* Large-scale single-cell analysis reveals critical immune characteristics of COVID-19 patients. *Biorxiv* 2020; : 2020.10.29.360479.

21 Schulte-Schrepping J, Reusch N, Paclik D, Baßler K, Schlickeiser S, Zhang B *et al.* Severe COVID-19 Is Marked by a Dysregulated Myeloid Cell Compartment. *Cell* 2020; **182**: 1419-1440.e23.

22 Sekine T, Perez-Potti A, Rivera-Ballesteros O, Strålin K, Gorin J-B, Olsson A *et al.* Robust T Cell Immunity in Convalescent Individuals with Asymptomatic or Mild COVID-19. *Cell* 2020; **183**: 158-168.e14.

23 Silvin A, Chapuis N, Dunsmore G, Goubet A-G, Dubuisson A, Derosa L *et al.* Elevated Calprotectin and Abnormal Myeloid Cell Subsets Discriminate Severe from Mild COVID-19. *Cell* 2020; **182**: 1401-1418.e18.

24 Song J-W, Zhang C, Fan X, Meng F-P, Xu Z, Xia P *et al.* Immunological and inflammatory profiles in mild and severe cases of COVID-19. *Nature Communications* 2020; **11**: 3410.

25 Wilk AJ, Rustagi A, Zhao NQ, Roque J, Martinez-Colon GJ, McKechnie JL *et al.* A single-cell atlas of the peripheral immune response in patients with severe COVID-19. *Nature medicine* 2020; **26**: 1070–1076.

26 Giamarellos-Bourboulis EJ, Netea MG, Rovina N, Akinosoglou K, Antoniadou A, Antonakos N *et al.* Complex Immune Dysregulation in COVID-19 Patients with Severe Respiratory Failure. *Cell Host Microbe* 2020; **27**: 992-1000.e3.

27 Merad M, Martin JC. Pathological inflammation in patients with COVID-19: a key role for monocytes and macrophages. *Nat Rev Immunol* 2020; **20**: 355–362.

28 Ong EZ, Chan YFZ, Leong WY, Lee NMY, Kalimuddin S, Mohideen SMH *et al.* A Dynamic Immune Response Shapes COVID-19 Progression. *Cell host & microbe* 2020; **27**: 879-882.e2.

29 Reizine F, Lesouhaitier M, Gregoire M, Pinceaux K, Gacouin A, Maamar A *et al.* SARS-CoV-2-Induced ARDS Associates with MDSC Expansion, Lymphocyte Dysfunction, and Arginine Shortage. *J Clin Immunol* 2021; **41**: 515–525.

30 Mudd PA, Crawford JC, Turner JS, Souquette A, Reynolds D, Bender D *et al.* Distinct inflammatory profiles distinguish COVID-19 from influenza with limited contributions from cytokine storm. *Sci Adv* 2020; **6**: eabe3024.

31 Biasi SD, Meschiari M, Gibellini L, Bellinazzi C, Borella R, Fidanza L *et al.* Marked T cell activation, senescence, exhaustion and skewing towards TH17 in patients with COVID-19 pneumonia. *Nat Commun* 2020; **11**: 3434.

32 Biasi SD, Tartaro DL, Meschiari M, Gibellini L, Bellinazzi C, Borella R *et al.* Expansion of plasmablasts and loss of memory B cells in peripheral blood from COVID□19 patients with pneumonia. *Eur J Immunol* 2020; **50**: 1283–1294.

33 Vabret N, Britton GJ, Gruber C, Hegde S, Kim J, Kuksin M *et al.* Immunology of COVID-19: Current State of the Science. *Immunity* 2020; **52**: 910–941.

34 Ranieri VM, Rubenfeld GD, Thompson BT, Ferguson ND, Caldwell E, Fan E *et al.* Acute respiratory distress syndrome: the Berlin Definition. *JAMA : the journal of the American Medical Association* 2012; **307**: 2526–2533.

35 Arvaniti E, Claassen M. Sensitive detection of rare disease-associated cell subsets via representation learning. *Nat Commun* 2017; **8**: 14825.

36 Galli E, Hartmann FJ, Schreiner B, Ingelfinger F, Arvaniti E, Diebold M *et al.* GM-CSF and CXCR4 define a T helper cell signature in multiple sclerosis. *Nat Med* 2019; **25**: 1290–1300.

37 Krieg C, Nowicka M, Guglietta S, Schindler S, Hartmann FJ, Weber LM *et al.* High-dimensional single-cell analysis predicts response to anti-PD-1 immunotherapy. *Nature medicine* 2018; **9**: 2579–14.

38 Bedin A-S, Makinson A, Picot M-C, Mennechet F, Malergue F, Pisoni A *et al.* Monocyte CD169 Expression as a Biomarker in the Early Diagnosis of Coronavirus Disease 2019. *J Infect Dis* 2020; **223**: 562–567.

39 Bourgoin P, Soliveres T, Barbaresi A, Loundou A, Belkacem IA, Arnoux I *et al.* CD169 and CD64 could help differentiate bacterial from CoVID□19 or other viral infections in the Emergency Department. *Cytom Part A* 2021. doi:10.1002/cyto.a.24314.

40 Ortillon M, Coudereau R, Cour M, Rimmelé T, Godignon M, Gossez M *et al.* Monocyte CD169 expression in COVID□19 patients upon intensive care unit admission. *Cytom Part A* 2021. doi:10.1002/cyto.a.24315.

41 Chevrier S, Levine JH, Zanotelli VRT, Silina K, Schulz D, Bacac M *et al.* An Immune Atlas of Clear Cell Renal Cell Carcinoma. *Cell* 2017; **169**: 736-738.e18.

42 Kuri-Cervantes L, Pampena MB, Meng W, Rosenfeld AM, Ittner CAG, Weisman AR *et al.* Comprehensive mapping of immune perturbations associated with severe COVID-19. *Sci Immunol* 2020; **5**: eabd7114.

43 Laing AG, Lorenc A, Barrio I del M del, Das A, Fish M, Monin L *et al.* A dynamic COVID-19 immune signature includes associations with poor prognosis. *Nat Med* 2020; **26**: 1623–1635.

44 Delano MJ, Ward PA. The immune system's role in sepsis progression, resolution, and long□term outcome. *Immunol Rev* 2016; **274**: 330–353.

45 Ferrando C, Suarez-Sipmann F, Mellado-Artigas R, Hernández M, Gea A, Arruti E *et al.* Clinical features, ventilatory management, and outcome of ARDS caused by COVID-19 are similar to other causes of ARDS. *Intens Care Med* 2020; **46**: 2200–2211.

46 Gattinoni L, Coppola S, Cressoni M, Busana M, Rossi S, Chiumello D. Covid-19 Does Not Lead to a "Typical" Acute Respiratory Distress Syndrome. *Am J Resp Crit Care* 2020; **0**: 1299–1300.

47 Carissimo G, Xu W, Kwok I, Abdad MY, Chan Y-H, Fong S-W *et al.* Whole blood immunophenotyping uncovers immature neutrophil-to-VD2 T-cell ratio as an early marker for severe COVID-19. *Nat Commun* 2020; **11**: 5243.

48 Farina A, Peruzzi G, Lacconi V, Lenna S, Quarta S, Rosato E *et al.* Epstein-Barr virus lytic infection promotes activation of Toll-like receptor 8 innate immune response in systemic sclerosis monocytes. *Arthritis Res Ther* 2017; **19**: 39.

49 Rempel H, Calosing C, Sun B, Pulliam L. Sialoadhesin expressed on IFN-induced monocytes binds HIV-1 and enhances infectivity. *PLoS ONE* 2008; **3**: e1967.

50 Carvelli J, Demaria O, Vély F, Batista L, Benmansour NC, Fares J *et al.* Association of COVID-19 inflammation with activation of the C5a–C5aR1 axis. *Nature* 2020; **588**: 146–150.

51 Liao M, Liu Y, Yuan J, Wen Y, Xu G, Zhao J *et al.* Single-cell landscape of bronchoalveolar immune cells in patients with COVID-19. *Nature medicine* 2020; **26**: 842–844.

52 Bastard P, Rosen LB, Zhang Q, Michailidis E, Hoffmann H-H, Zhang Y *et al.* Autoantibodies against type I IFNs in patients with life-threatening COVID-19. *Science* 2020; **370**: eabd4585.

53 Zhang Q, Bastard P, Liu Z, Pen JL, Moncada-Velez M, Chen J *et al.* Inborn errors of type I IFN immunity in patients with life-threatening COVID-19. *Science* 2020; **370**: eabd4570.

54 Galbraith MD, Kinning KT, Sullivan KD, Baxter R, Araya P, Jordan KR *et al.* Seroconversion stages COVID19 into distinct pathophysiological states. *Elife* 2021; **10**: e65508.

55 Stolk RF, Pasch E van der, Naumann F, Schouwstra J, Bressers S, Herwaarden AE van *et al.* Norepinephrine Dysregulates the Immune Response and Compromises Host Defense during Sepsis. *Am J Resp Crit Care* 2020; **202**: 830–842.

56 Reyes M, Filbin MR, Bhattacharyya RP, Sonny A, Mehta A, Billman K *et al.* Induction of a regulatory myeloid program in bacterial sepsis and severe COVID-19. *Biorxiv* 2020; : 2020.09.02.280180.

57 Thompson EA, Cascino K, Ordonez AA, Zhou W, Vaghasia A, Hamacher-Brady A *et al.* Mitochondrial induced T cell apoptosis and aberrant myeloid metabolic programs define distinct immune cell subsets during acute and recovered SARS-CoV-2 infection. *Medrxiv Prepr Serv Heal Sci* 2020. doi:10.1101/2020.09.10.20186064.

58 Xu G, Qi F, Li H, Yang Q, Wang H, Wang X *et al.* The differential immune responses to COVID-19 in peripheral and lung revealed by single-cell RNA sequencing. *Cell Discov* 2020; **6**: 73.

59 Sánchez-Cerrillo I, Landete P, Aldave B, Sánchez-Alonso S, Sánchez-Azofra A, Marcos-Jiménez A *et al.* COVID-19 severity associates with pulmonary redistribution of CD1c+ DC and inflammatory transitional and nonclassical monocytes. *J Clin Invest* 2020; **130**: 6290–6300.

60 Fan E, Beitler JR, Brochard L, Calfee CS, Ferguson ND, Slutsky AS *et al.* COVID-19-associated acute respiratory distress syndrome: is a different approach to management warranted? *Lancet Respir Medicine* 2020; **8**: 816–821.

61 Levey AS, Eckardt K-U, Tsukamoto Y, Levin A, Coresh J, Rossert J *et al.* Definition and classification of chronic kidney disease: A position statement from Kidney Disease: Improving Global Outcomes (KDIGO). *Kidney Int* 2005; **67**: 2089–2100.

62 Ponikowski P, Voors AA, Anker SD, Bueno H, Cleland JGF, Coats AJS *et al.* 2016 ESC Guidelines for the diagnosis and treatment of acute and chronic heart failureThe Task Force for the diagnosis and treatment of acute and chronic heart failure of the European Society of Cardiology (ESC)Developed with the special contribution of the Heart Failure Association (HFA) of the ESC. *Eur Heart J* 2016; **37**: 2129–2200.

63 Gall JRL. A new Simplified Acute Physiology Score (SAPS II) based on a European/North American multicenter study. *Jama J Am Medical Assoc* 1993; **270**: 2957–2963.

64 Gaudriot B, Uhel F, Gregoire M, Gacouin A, Biedermann S, Roisne A *et al.* Immune Dysfunction After Cardiac Surgery with Cardiopulmonary Bypass. *Shock* 2015; **44**: 228–233.

65 Balc'h PL, Pinceaux K, Pronier C, Seguin P, Tadié J-M, Reizine F. Herpes simplex virus and cytomegalovirus reactivations among severe COVID-19 patients. *Crit Care* 2020; **24**: 530.

Highlights

- Machine-learning analysis of CyTOF data segregates Covid-19^{+} and Covid-19^{-} ARDS
- CD169^{+}S100A9^{+} monocytes differentiate Covid-19 ARDS from other ARDS
- Monocyte compartment alterations correlate with other immune subset modifications
- CD14^{+}HLA-DR^{lo} and CD14^{lo}CD16^{+} monocytes are markers of adverse Covid-19 evolution

eTOC Blurb

Roussel et al. characterize the immune profile of COVID-19^{+} and COVID-19^{-} patients, both presenting an acute respiratory distress syndrome (ARDS) and COVID-19^{+} without ARDS. They identify a COVID-19 signature associating CD169^{+}S100A9^{+} monocytes, plasmablasts, and Th1 cells. CD14^{+}HLA-DR^{lo} and CD14^{lo}CD16^{+} monocytes increase during the ICU stay correlate with unfavorable clinical course.

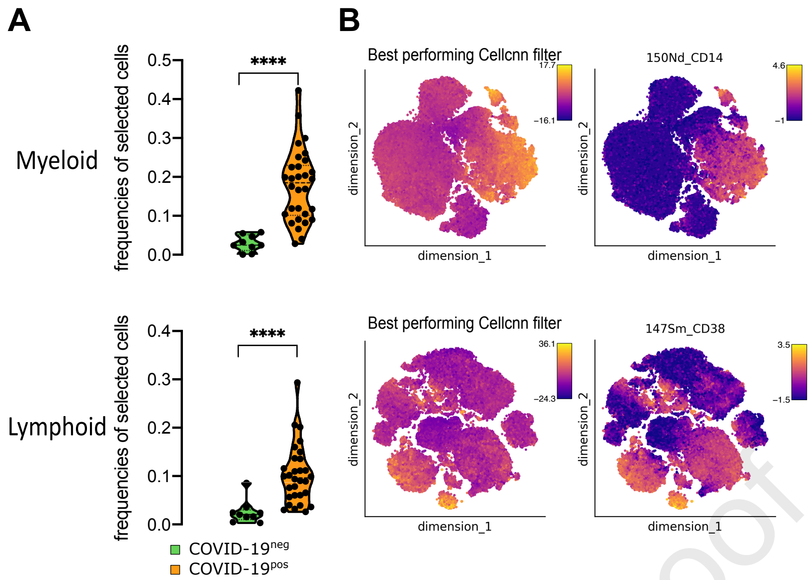
A
B
Myeloid
Lymphoid
frequencies of selected cells
****
COVID-19neg
COVID-19pos
Best performing Cellcnn filter
150Nd_CD14
147Sm_CD38
dimension_1
dimension_2

Figure 1

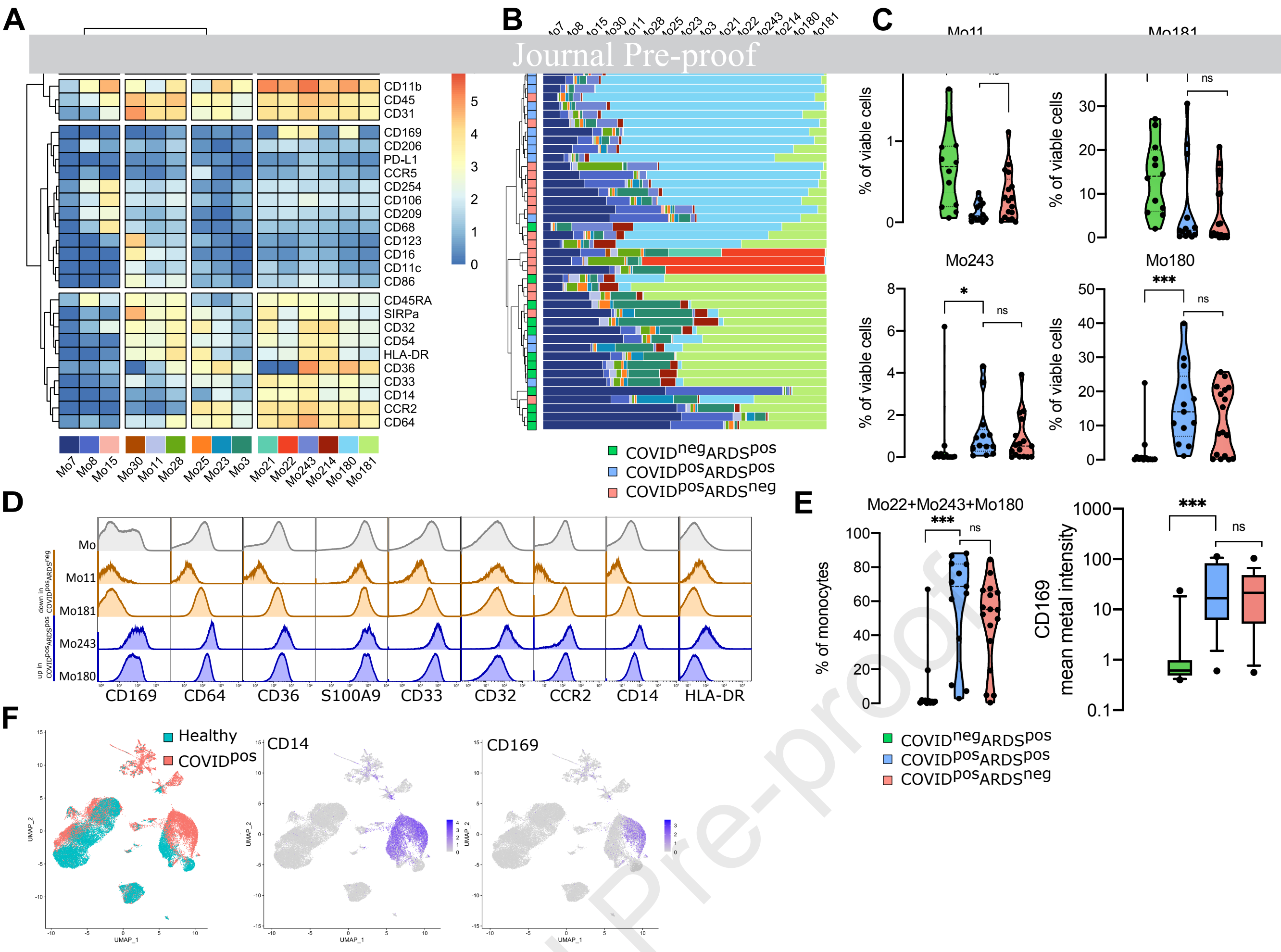
A
CD11b
CD45
CD31
CD169
CD206
PD-L1
CCR5
CD254
CD106
CD209
CD68
CD123
CD16
CD11c
CD86
CD45RA
SIRPa
CD32
CD54
HLA-DR
CD36
CD33
CD14
CCR2
CD64
Mo7
Mo8
Mo15
Mo30
Mo11
Mo28
Mo25
Mo23
Mo3
Mo21
Mo22
Mo243
Mo214
Mo180
Mo181
B
COVIDnegARDSpos
COVIDposARDSpos
COVIDposARDSneg
C
Mo11
Mo181
Mo243
Mo180
% of viable cells
ns
*
***
D
Mo
Mo11
Mo181
Mo243
Mo180
CD169
CD64
CD36
S100A9
CD33
CD32
CCR2
CD14
HLA-DR
E
Mo22+Mo243+Mo180
% of monocytes
CD169 mean metal intensity
F
Healthy
COVIDpos
CD14
CD169
UMAP_1
UMAP_2

Figure 2

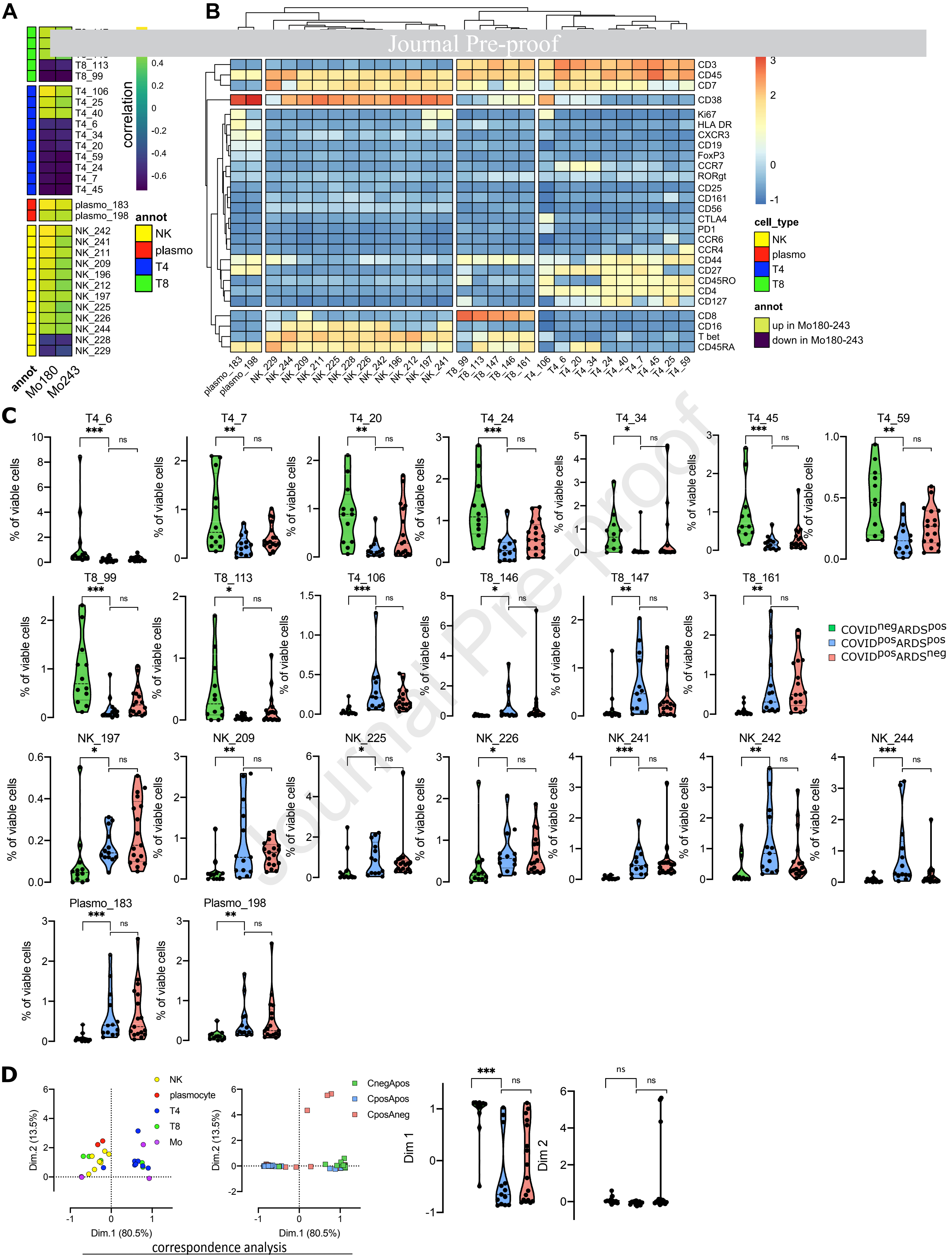

A
B
C
D
correlation
annot
NK
plasmo
T4
T8
cell_type
up in Mo180-243
down in Mo180-243
% of viable cells
COVIDnegARDSpos
COVIDposARDSpos
COVIDposARDSneg
Dim.1 (80.5%)
Dim.2 (13.5%)
correspondence analysis
CnegApos
CposApos
CposAneg
Dim 1
Dim 2

Figure 3

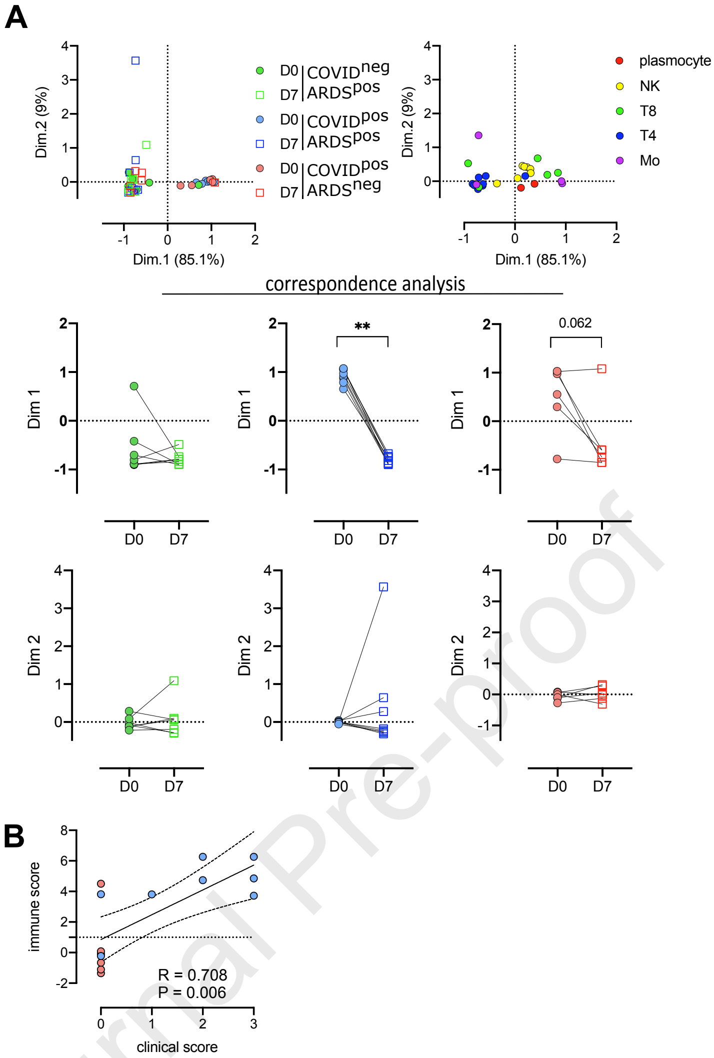
A
Dim.2 (9%)
Dim.1 (85.1%)
D0
D7
COVIDneg
ARDSpos
COVIDpos
ARDSpos
COVIDpos
ARDSneg
plasmocyte
NK
T8
T4
Mo
correspondence analysis
Dim 1
Dim 2
D0
D7
**
0.062
B
immune score
clinical score
R = 0.708
P = 0.006

Figure 4